Catalysis Science & Technology

ROYAL SOCIETY OF CHEMISTRY

PAPER

View Article Online
View Journal | View Issue

Cite this: *Catal. Sci. Technol.*, 2026, **16**, 3190

Hydrogenation of cinnamaldehyde by platinum supported on 2D and 3D transition metal sulfides

Ayesha Shafiq, [a] Iryna Danylo, [a] Lukas Kolacny, [a] Berke Sevemez, [a] Jan Luxa, [b] Martin Vesely [a] and Martina Pitinova *[a]

Received 11th December 2025,
Accepted 12th March 2026

DOI: 10.1039/d5cy01520k

rsc.li/catalysis

The selective hydrogenation of cinnamaldehyde (CAL), a model α,β-unsaturated aldehyde, yields valuable products such as cinnamyl alcohol (COL) and hydrocinnamaldehyde (HCAL). Pt-based catalysts supported on transition metal dichalcogenides (MoS_2, WS_2, and their composite) in bulk forms and their exfoliated counterparts were synthesized using microwave-assisted and wet impregnation methods. Characterization (SEM/EDS, TEM, XRF, XRD, and BET) confirmed ~9 wt% Pt loading, preserved layered structures, and well-dispersed nanoparticles. Catalysts based on 2D supports provided finer Pt dispersion (2–6 nm), with microwave synthesis yielding smaller, more uniform particles, especially in the Mo–W composite. Catalytic testing demonstrated that both activity and selectivity were strongly influenced by the support composition and morphology, with the 2D Mo–W composite outperforming MoS_2 and WS_2. All catalysts predominantly promoted selective C=O hydrogenation to COL, while HCAL and HCOL remained minor products. The best performance was achieved with Pt supported on the 2D Mo–W–S composite prepared by microwave-assisted synthesis, delivering 75% CAL conversion with a COL selectivity and yield of 64% and 48%, respectively, achieved within 6 h.

Introduction

The selective hydrogenation of α,β-unsaturated aldehydes is a key route to unsaturated alcohols used in pharmaceuticals, fragrances, and food additives. Cinnamaldehyde (CAL), a model compound with an aromatic ring and C=C and C=O groups, produces three main hydrogenation products, with cinnamyl alcohol (COL) being the most valuable intermediate. Its transformation is surface-catalyzed and strongly influenced by catalyst properties, reaction conditions, and adsorption behavior. Cinnamaldehyde (CAL) hydrogenation proceeds *via* two main pathways, selective C=O hydrogenation forming cinnamyl alcohol (COL) or C=C hydrogenation yielding hydrocinnamaldehyde (HCAL).[1] Both of these groups further hydrogenate to form the final product hydrocinnamyl alcohol (HCOL) as shown in the reaction scheme (Fig. 1). The HCAL pathway is thermodynamically more favorable because of the lower bond energy of the alkene group (615 kJ mol^{-1}) compared to the carbonyl group (715 kJ mol^{-1}) and the η^4 adsorption mode.[2]

While HCAL serves as an intermediate in pharmaceutical synthesis, particularly for HIV treatments,[3] COL is the preferred product because of its broad applications in pharmaceuticals, fragrances, fine chemicals, and the food industry.[4,5] Therefore, although thermodynamics favors (C=C) hydrogenation toward HCAL, achieving high selectivity toward COL requires precise control of catalyst surface properties and adsorption modes.

Consequently, significant research efforts have been directed toward designing catalysts that selectively hydrogenate the carbonyl (C=O) group while preserving the carbon–carbon double bond (C=C). Product distribution in cinnamaldehyde (CAL) hydrogenation depends on the catalyst type, solvent, additives, and reaction conditions. Selectivity is closely related to the d-bandwidth of the metal catalyst, as greater orbital extension enhances cinnamyl alcohol (COL) formation. Metals with large d-bandwidths such as Pt, Ru, and Ir are therefore commonly employed. Over recent decades, both homogeneous and heterogeneous catalytic systems have been explored to address this selectivity challenge.[6] Homogeneous catalysts offer high selectivity through ligand-controlled steric and electronic effects but face limitations such as difficult separation, low reusability, and possible contamination, which restrict practical applications.[7] To overcome these issues, extensive research has focused on developing heterogeneous catalysts using both noble and non-noble metals. Literature reports highlight the use of noble metal-based catalysts, including Pt, Pd, Au, and Ru, for efficient cinnamaldehyde (CAL)

[a] *Department of Organic Technology, University of Chemistry and Technology, 166 28 Prague, Czech Republic. E-mail: Martina.Pitinova@vscht.cz*
[b] *Department of Inorganic Chemistry, University of Chemistry and Technology, 166 28 Prague, Czech Republic*

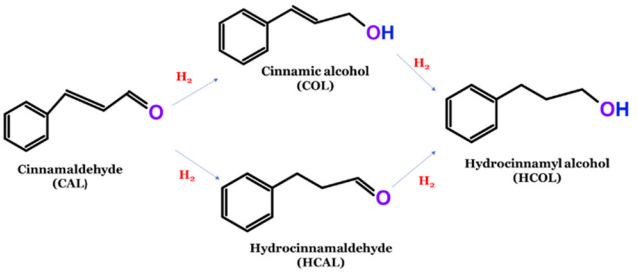

Fig. 1 Scheme of cinnamaldehyde (CAL) hydrogenation to cinnamyl alcohol (COL), hydrocinnamaldehyde (HCAL), and hydrocinnamyl alcohol (HCOL).

hydrogenation.[8–11] Non-noble metal catalysts such as Co, Cu, and Ni have also been explored for CAL hydrogenation.[12–15] Yuan *et al.*[16] reported that bimetallic CoPt nanoparticles supported on Fe_3O_4 achieved 95% CAL conversion with 84% selectivity to COL. In contrast, Cu-based catalysts showed poor conversion and selectivity.[17] Ni-based systems generally favored HCAL formation, as Mohire *et al.*[18] achieved 100% HCAL selectivity at 89% CAL conversion using a Ni–Cu–RGO catalyst. Similarly, Pd-based catalysts tend to promote C=C bond hydrogenation, leading to higher HCAL yields; for instance, Chen *et al.*[19] developed Pd nanoparticles encapsulated in a mesoporous carbon matrix, producing HCAL as the main product with 80% selectivity. Product selectivity in CAL hydrogenation is influenced not only by the choice of metal but also by the solvent, support, and catalyst morphology. The preparation method and nanoparticle distribution play a critical role as well.[20,21] The location of Ru nanoparticles on carbon nanotubes (CNTs) strongly affected CAL hydrogenation selectivity; Ru encapsulated within CNT channels favored C=O hydrogenation due to confinement effects, while Ru deposited on the outer CNT walls promoted preferential C=C hydrogenation.[22] Gold (Au) and iridium (Ir)-based catalysts have also been investigated for CAL hydrogenation. In the case of Au, COL selectivity varied widely (10–90%) when uniform nanoparticles were supported on different oxides such as MgO, Al_2O_3, TiO_2, Fe_2O_3, Co_3O_4, ZnO, and In_2O_3, strongly influenced by the acidic or basic nature of the oxide supports.[23]

Among the noble metals investigated, platinum-based catalysts have emerged as particularly promising systems due to their tuneable electronic structure and strong metal–support interactions. Platinum-based (Pt) catalysts are highly effective in the selective hydrogenation of cinnamaldehyde (CAL), generally favoring cinnamyl alcohol (COL) as the main product. However, their high activity can also cause over-hydrogenation to hydrocinnamyl alcohol (HCOL), since Pt promotes both C=O and, to some extent, C=C bond hydrogenation. To enhance COL selectivity and suppress over-hydrogenation, a range of Pt-based monometallic and bimetallic catalysts have been developed,[24–28] achieving over 90% CAL conversion with more than 90% COL selectivity. These improvements rely on strategies such as optimizing support materials, controlling Pt size and dispersion, adjusting reaction conditions, and tailoring metal–support interactions to guide the reaction pathway. Product selectivity, however, can still vary within the same catalytic system depending on the reaction conditions and support morphology. Wei *et al.*[29] demonstrated structure-dependent selectivity in Pt/CeO_2–ZrO_2 catalysts, where changes in the Ce : Zr molar ratio significantly influenced COL selectivity, highlighting the key role of Pt–support interactions. Despite these advances, achieving consistent and controllable selectivity toward COL remains challenging, as product distribution strongly depends on metal dispersion, electronic properties, and support effects. In this context, exploring novel support materials capable of modulating the Pt electronic structure and adsorption behaviour represents a promising strategy.

Although significant progress has been achieved with oxide, carbon, and metal-supported catalysts, several challenges remain, particularly regarding the role of the support in governing adsorption behaviour and reaction selectivity. In a recent study, Wang *et al.* systematically investigated a series of Pt catalysts supported on different metal oxides (Pt/MO_x) for the selective hydrogenation of cinnamaldehyde (CAL). Their results clearly demonstrated that the nature of the support plays a decisive role in determining both catalytic activity and product selectivity. Specifically, Mn_2O_3 and Fe_2O_3 were identified as favourable supports for preferential adsorption of the C=O functional group, thereby promoting selective hydrogenation toward the unsaturated alcohol. In contrast, TiO_2 exhibited a stronger interaction with the C=C bond, as evidenced by FTIR analysis, leading to a shift in selectivity toward C=C hydrogenation products.[30] These findings highlight the critical influence of support properties on substrate adsorption modes and, consequently, on chemoselectivity in CAL hydrogenation. In another study, Patil *et al.* in their review briefly discussed catalyst design strategies for selective CAL hydrogenation, highlighting the influence of the metal type, preparation method, and structural properties on chemoselectivity toward COL or HCAL.[31]

In this context, exploring alternative support materials that can modulate metal–support interactions in a more controlled and effective manner becomes highly relevant. Two-dimensional (2D) transition metal dichalcogenides (TMDs) have gained considerable interest due to their unique chemical, electronic, mechanical, and magnetic properties. Their multifunctionality makes them promising for applications in spintronics, optoelectronics, sensing, catalysis, and energy-related technologies.[32,33] MoS_2 has been widely explored as a support for various metals such as Fe, Co, Ni, Cu, Ru, Rh, Pd, and Ag in CO_2 hydrogenation.[34] Pt has also been effectively integrated with MoS_2, for instance, Pt monomers anchored on MoS_2 nanosheets achieved a high loading of 7.5% while maintaining atomic dispersion, where synergistic interactions between adjacent Pt monomers greatly enhanced CO_2 hydrogenation performance.[35] Similarly, Xu *et al.*[36] deposited Pt on MoS_2 *via* a wet impregnation method to study

hydrogen evolution reaction (HER) kinetics and reported superior performance of the Pt–MoS_2 system compared to Pt/C. Although transition metal dichalcogenide (TMD)-supported metals have demonstrated remarkable performance in hydrogenation reactions such as CO_2 conversion and HERs, their potential in hydrogenation of α,β-unsaturated aldehydes remains largely unexplored. Various synthesis techniques have been employed to tune Pt nanoparticle size and density, including electron beam lithography for fabricating Pt-based 2D materials.[37] Many reported systems involve complex synthesis procedures.[38] In this study, we systematically investigate Pt–TMD catalysts synthesized by simple preparation methods including *via* microwave-assisted and wet impregnation methods, supported on MoS_2, WS_2, and Mo–W–S composites in both bulk (3D) and nanosheet (2D) forms. By directly comparing the morphology, composition, and synthesis route, this work establishes structure–selectivity relationships and demonstrates the advantages of TMD supports over traditional systems in controlling catalytic activity and product distribution.

Experimental

Materials

Cinnamaldehyde (*trans*-cinnamaldehyde, 97%) and chloroplatinic acid hexahydrate ($H_2PtCl_6{\cdot}6H_2O$) were supplied by Merck KGaA (Darmstadt, Germany), ethylene glycol (G. R.) and isopropyl alcohol (G. R., iso reagent) were supplied by Lach-Ner, s.r.o. (Neratovice, Czech Republic), and mesitylene (purity., >99.0%) was supplied by Fluka (Buchs, Switzerland). Granulated sulphur (99.999%), molybdenum powder (99.95%, −100 mesh), and tungsten powder (99.9%, −100 mesh) were obtained from Strem, USA. 5% Pt/alumina was obtained from Johnson Matthey (123 powder, Royston, United Kingdom).

Synthesis of layered transition metal dichalcogenides

Molybdenum disulfide (MoS_2), tungsten disulfide (WS_2) and their composite ($Mo_{0.25}W_{0.75}S_2$) were synthesized by reacting powdered metals with elemental chalcogens in vacuum sealed quartz ampoules, followed by controlled thermal treatments reported by Sofer *et al.*[39] Transition metals and chalcogens were weighed in stoichiometric ratios (±1 mg) to prepare 10 g of transition metal dichalcogenide (TMD), with an additional 30 mg of chalcogen added to ensure excess. The mixture was sealed in an evacuated ampoule (pressure $<5 \times 10^5$ mbar) and preheated with a 300 °C heat gun for 2 minutes. The ampoules were then melt-sealed using an oxygen–hydrogen torch. The sealed ampoules were heated at 425 °C for 24 hours in a muffle furnace, followed by a gradual temperature increase to 500 °C over 24 hours and subsequent cooling. After 10 minutes of mechanical homogenization, the samples were heated at 600 °C for 48 hours (heating/cooling rate: 5 °C/0.0167 h). A second homogenization step was followed by heating at 800 °C for 48 hours, and then 850 °C for 12 hours under the same rate conditions. For MoS_2, the final step was modified to 700 °C for 72 hours to prevent 3R phase formation. Excess chalcogen was removed by heating one end of the ampoule to 600 °C for 30 minutes while keeping the other end at room temperature.

Catalyst preparation

Catalysts were synthesized using bulk TMDs (MoS_2, WS_2 and Mo–W–S) and their 2D counterparts *via* two distinct methods, simple wet impregnation and microwave-assisted impregnation, both with *in situ* chemical reduction.[40] In both approaches, an impregnation mixture was prepared by mixing 272.7 mL of ethylene glycol (reducing agent), 27.2 mL of deionized water (solvent), 1.56 mL of 0.04 M $H_2PtCl_6{\cdot}6H_2O$ solution (Pt precursor), and 120 mg of support material (MoS_2, WS_2 or Mo–W–S). A nominal Pt loading of 9.2 wt% was applied to all catalysts. A deliberately high Pt content was selected to clearly isolate and quantify the promotional effect of Pt on catalytic performance, ensuring that any observed activity trends could be attributed unambiguously to Pt rather than to support-related limitations.

Wet impregnation with chemical reduction. The impregnation mixture was first subjected to ultrasonic treatment for 4 hours to ensure additional exfoliation of 2D nanosheets (in the case of 2D analogues of TMDs) and uniform dispersion of Pt NPs over the support. It was then transferred to an oil bath and stirred under reflux (120 °C, oil bath) for 20 hours. After cooling, the resulting catalyst was filtered, washed with deionized water, and dried in a vacuum oven at 60 °C for 24 hours. Activation of the prepared catalysts was carried out by reduction in a calcination oven under a stream of hydrogen and nitrogen (H_2/N_2 = 40/60 (v/v)) at 250 °C for 2 h (temperature ramp of 250 °C/360 min) prior to testing in the hydrogenation reaction.

Microwave-assisted wet impregnation with chemical reduction. The prepared impregnation mixture was placed in a microwave oven (UWave-2000 Multifunctional Microwave Chemistry Reaction Workstation, Sineo) and irradiated for 4 minutes (500 W), followed by a 4 minute rest period. The temperature was maintained at 80 °C for 12 minutes, increasing slightly to 86 °C due to continuous sonication. The mixture was also subjected to ultrasonic treatment for 21 minutes and 40 seconds to enhance exfoliation (in the case of 2D nanosheets) and enhance Pt dispersion. After this impregnation process, the catalyst was treated as in the case of simple wet impregnation, filtration, washing, drying and reduction (a stream of hydrogen and nitrogen gas H_2/N_2 = 40/60 (v/v) at 250 °C for 2 h). For better understanding, Table 1 provides description about the used supports for catalyst preparation, preparation methods and catalyst labelling.

Cinnamaldehyde hydrogenation

For hydrogenation, a high pressure autoclave Parr (volume 100 mL) was used in batch mode. 2.7 g of cinnamaldehyde (reactant) was mixed with 50 mL of isopropyl alcohol

Table 1 Pt-based catalysts prepared using various supports and their preparation methods

Support	Support	Preparation method	Catalyst label
MoS_2	2D	WIR	Pt/2D-MoS_2-WIR
		MW	Pt/2D-MoS_2-MW
	3D	WIR	Pt/3D-MoS_2-WIR
		MW	Pt/3D-MoS_2-MW
WS_2	2D	WIR	Pt/2D-WS_2-WIR
		MW	Pt/2D-WS_2-MW
	3D	WIR	Pt/3D-WS_2-WIR
		MW	Pt/3D-WS_2-MW
Mo–W–S	2D	WIR	Pt/2D-Mo–W–S-WIR
		MW	Pt/2D-Mo–W–S-MW
	3D	WIR	Pt/3D-Mo–W–S-WIR
		MW	Pt/3D-Mo–W–S-MW

Note: 3D = bulk, 2D = nano, WIR = wet impregnation with chemical reduction, and MW = microwave-assisted impregnation with chemical reduction.

(solvent) and 400 μL of mesitylene (internal standard for GC analysis). A zero sample was taken before starting the reaction. Subsequently, 27 mg of catalyst was then added to the reaction mixture and sealed in the autoclave. Before pressurizing the system, the autoclave was flushed three times with nitrogen and once with hydrogen. The reaction was performed under 1 MPa hydrogen pressure, at a temperature of 80 °C, and stirred at 800 rpm.

The progress of the reaction was observed by analyzing samples at set interval times (30, 60, 120, 240 and 360 minutes) taken *via* capillary sampling. The reaction was performed for a maximum of 360 minutes. Before subjecting to GC, the samples were centrifuged at 8000 rpm for 5 minutes, and the supernatant was further filtered and analyzed using GC (SHIMADZU GC 2014 with an FID and a capillary column SPB5 with a length of 30 m, a width of 0.32 mm and a stationary phase of 0.25 μm).

The evaluated catalysts were assessed based on their activity, measured by conversion after 360 minutes and the achieved selectivities toward hydrogenation products.

Conversion of cinnamaldehyde (%):

$$X_t = \frac{C_{\mathrm{CAL},0} - C_{\mathrm{CAL},t}}{C_{\mathrm{CAL},0}} \times 100\% \quad (1)$$

Selectivity toward products (%):

$$S_t = \frac{n_{t,t}}{\sum n_{\mathrm{products},t}} \times 100\% \quad (2)$$

Reaction rates (mmol min^{-1} mg_{Pt}^{-1}):

$$r_0 = \frac{C_{\mathrm{CAL},0} - C_{\mathrm{CAL},t_1}}{t_1 \times \mathrm{mg_{Pt}}} \times L \quad (3)$$

$$r_t = \frac{C_{\mathrm{CAL},t_2} - C_{\mathrm{CAL},t_3}}{(t_3 - t_2) \times \mathrm{mg_{Pt}}} \times L \quad (4)$$

Turn over frequency was calculated using equations given below.

Moles of CAL converted:

$$r_{\mathrm{avg}} = \frac{(n_{\mathrm{CAL},0} - n_{\mathrm{CAL},t}) \times V}{t} \quad (5)$$

Moles of Pt:

$$n_{\mathrm{Pt}} = \frac{m_{\mathrm{cat}} \times \omega_{\mathrm{M}}}{\mathrm{MW_m}} \quad (6)$$

Pt dispersion from TEM:

$$D = \left(3.32 \times \frac{d_{\mathrm{Pt}}}{d_{\mathrm{p}}}\right)^{0.813} \quad (7)$$

$$n_{\mathrm{Pt,surface}} = D \times n_{\mathrm{Pt}} \quad (8)$$

Turn over frequency:

$$\frac{r_{\mathrm{avg}}}{n_{\mathrm{Pt,surface}}} \quad (9)$$

In the equations, $c_{\mathrm{CAL},0}$ and $c_{\mathrm{CAL},t}$ are the initial and actual concentrations of cinnamaldehyde (mmol L^{-1}), $c_{i,t}$ is the actual concentration of the selected product (mmol L^{-1}), $n_{i,t}$ is the actual number of moles of the selected product (mmol), t is the reaction time (min), t_1 is the reaction time for calculating the initial reaction rate (30 min in this case, which is the time for taking the first sample), r_o is the initial reaction rate (mmol min^{-1} mg_{Pt}^{-1}), and r_t is the reaction rate at higher reaction times (mmol min^{-1} mg_{Pt}^{-1}). The rates of reactions were calculated with considering catalyst mass and metal loadings. Turn over frequency was calculated using the number of moles of cinnamaldehyde converted at 360 minutes and surface dispersion of platinum nanoparticles using the average diameter obtained from TEM analysis (eqn (5)–(9)). In eqn (5), $n_{\mathrm{CAL},t}$ is the molar concentration of cinnamaldehyde at 360 minutes. In eqn (6), m_{cat} is the amount of catalyst used in the reaction (g), ω_{M} is the metal loading in the catalyst (from XRF), and $\mathrm{MW_m}$ is the molecular mass of platinum. Platinum dispersion on the surface was calculated using eqn (7),[41] where d_{Pt} is the platinum atomic diameter (0.277 nm), and d_{p} is the average size of nanoparticles obtained from TEM.

Catalyst characterization

All catalysts were characterized in their final active form – after the reduction at 250 °C in a hydrogen atmosphere.

Scanning electron microscopy (SEM) and energy dispersive spectroscopy (EDS) were used for identification of the surface morphology and elemental composition of the catalysts. SEM images were obtained using a TESCAN LYRA3 GMU dual-beam scanning electron microscope (TESCAN, Brno, Czech Republic) equipped with a field emission gun (FEG). Elemental analysis and radial profile measurements were performed with an energy-dispersive X-ray spectrometer (EDS) featuring an 80 mm^2 SDD (X-MaxN, Oxford Instruments, Abingdon, Oxfordshire, England), processed using AZtecEnergy software. Quantitative elemental analysis

of the prepared and reduced catalysts was performed using a fully automatic sequential X-ray fluorescence spectrometer (XRF) Axios (PANalytical, Holland). The XRF spectrometer was equipped with a Rh tube, a 4 kW generator, 3 collimators, 8 crystals (PX1, PX4a, PX5, PX7, PE002, Ge 111, LiF 200, and LiF 220) and 2 detectors – proportional and scintillation. Standardless analysis was conducted with program Omnian. After synthesizing the catalyst, the reaction mixture was filtered to separate the solid catalyst. The collected filtrate was subsequently analysed using an Agilent 5900 ICP-OES (inductively coupled plasma optical emission spectrometer) to determine the extent of platinum (Pt) loss during the filtration process. The plasma was formed in a flow of Ar gas by an externally applied radio frequency field of 1.2 kW. The measurement was conducted in synchronous vertical dual view (SVDV) mode, allowing both the axial and radial views of the plasma to be captured in one reading, allowing fast but very accurate analysis. The quantitative analysis was allowed by the use of a 5-point calibration curve for each element measured. The measurement used an inner standard of yttrium at a wavelength of 371.029 nm. Each sample was measured in 3 duplicates with a 5 s reading time each. Spectral intensities for Pt were measured at a wavelength of 214.424. The measured values were obtained using the ICP Expert Pro software. Following filtration, the catalyst retained on the filter paper was washed three times with distilled water to ensure the removal of any residual soluble species. The combined washing solutions were subsequently subjected to analysis by atomic absorption spectrometry (AAS) in order to evaluate whether any platinum loss had occurred during the washing step. The measurements were performed using an Agilent 280FS AA spectrometer equipped with flame atomization. For platinum determination, an acetylene–air flame was applied at a wavelength of 265.9 nm.

Transmission electron microscopy was used for particle size measurement. Images were acquired by EFTEM with the Jeol 2200 FS specification (JEOL, Tokyo, Japan). The crystallinity of the prepared catalysts was analyzed using the X-ray diffraction (XRD) method. Measurements were conducted at room temperature with a Bruker-Phaser 2nd Generation powder diffractometer, utilizing CuKα radiation (λ[CuK-α1] = 1.54056 × 10^{-1} nm and λ[CuK-α2] = 1.54443 × 10^{-1} nm). Data acquisition was performed using a high-speed 1D PIXCEL detector over a 2θ range of 4.99–90.019°, with a time step of 0.5 s, resulting in a total scan time of 886.4 s. The collected data were analyzed using HighScore Plus software. The specific surface areas of the prepared and reduced catalysts were determined *via* nitrogen adsorption–desorption measurements using a NOVA 2000e surface area and pore size analyzer (Quantachrome Instruments, Anton Paar GmbH – Headquarters, Graz, Austria). Helium was used for the calibration of the measuring cells. The samples were outgassed at 150 °C for 3 h before each measurement. The BET equation was used for calculating the specific surface area of the catalysts.

XPS measurements were performed with an ESCA Probe P (electron spectroscopy for chemical analysis) instrument (from Omicron Nanotechnology Ltd., 2005) with a monochromatic Al-Kα X-ray source (1486.6 eV), operating at 15 kV and 105 W, and with a hemispherical analyzer. The operating vacuum was kept at ~5 × 10^{-10} mbar inside the analysis chamber. Calibration was performed using binding energies of Cu $2p_{3/2}$ (932.7 eV) and Ag $3d_{5/2}$ (368.26 eV), with full width at half maximum (FWHM) values for Cu $2p_{3/2}$ (0.85 eV) and Ag $3d_{5/2}$ (0.67 eV). For all samples were recorded survey and high-resolution scans of C 1s, O 1s, Pt 4f, Mo 3d, W 4f and S 2p. A compromise between resolution and acquisition time is obtained when a pass energy of 50 eV resp. 30 eV, step 0.4 resp. 0.1 eV was used for survey resp. high resolution scans. The surface charges during the XPS spectra acquisition were corrected by applying a very small current on the surface using a flood gun emission system. Etching of the surface film was conducted using XPS to obtain information about the nature of the oxide film. The spectra were evaluated using CasaXPS software 2.3.13Dev10, employing Shirley background subtraction and Gaussian–Lorentzian functions (GL(30)). An adventitious carbon C 1s peak at 285.3 eV was used for calibration of the spectra (to correct the position).

Results and discussion

The current study focuses on the use of MoS_2, WS_2 and their composite Mo–W–S in their bulk and 2D exfoliated forms, as support materials for the preparation of Pt-based catalysts. Furthermore, this work focuses on the evaluation of these catalytic supports in CAL hydrogenation. As mentioned in the Introduction, the preparation method can influence the physicochemical properties of the resulting catalysts and, consequently, affect catalytic activity. Therefore, two preparation methods were employed for catalyst synthesis: simple wet impregnation and a microwave-assisted technique, both conducted in the presence of ethylene glycol as a reducing agent.

X-ray fluorescence (XRF)

To evaluate the efficiency of the different preparation techniques and to determine the elemental composition of the samples, with particular emphasis on the actual platinum loading, X-ray fluorescence (XRF) analysis was employed. The results obtained from XRF are summarized in Table 2. The nominal Pt loading was fixed at 9.2 wt% for all the prepared catalysts. For the MoS_2-based catalysts, the actual Pt loading closely matched the targeted value. The MoS_2-supported catalysts exhibited higher Pt loadings than the other supports within the study, regardless of the synthesis method. In contrast, for WS_2, the wet impregnation reduction (WIR) method yielded a Pt content of 9.0 wt%, which is in good agreement with the nominal loading, whereas the microwave-assisted (MW) method proved unsuitable for this support. Only low Pt contents were obtained for the bulk and 2D WS_2

Table 2 XRF results for Pt supported on bulk and nanosheet analogues of MoS_2, WS_2, and Mo–W–S

	XRF elemental composition (wt%)				
Catalyst	Pt	Mo	W	S	Others
MoS_2	—	54	—	29	16
Pt/2D-MoS_2-MW	10.5	52	0	26	11
Pt/2D-MoS_2-WIR	10.5	52	0	27	10
Pt/3D-MoS_2-MW	10.0	50	0	26	11
Pt/3D-MoS_2-WIR	10.5	52	0	25	11
WS_2	—	—	75	24	x
Pt/2D-WS_2-MW	3.6	0	73	23	x
Pt/2D-WS_2-WIR	9.0	0	71	20	x
Pt/3D-WS_2-MW	1.2	0	77	21	x
Pt/3D-WS_2-WIR	8.7	0	76	16	x
Pt/2D-MoW-S-MW	7.5	10	59	23	x
Pt/2D-Mo–W–S-WIR	8.1	10	59	23	x
Pt/3D-Mo–W–S-MW	6.4	10	60	23	x
Pt/3D-Mo–W–S-WIR	8.7	10	59	22	x

analogues, namely 1.2 wt% and 3.6 wt%, respectively. This suggests that Pt is more easily and strongly bonded to the MoS_2 support than to WS_2. Similarly, in the Mo–W–S-based catalysts, the Pt loading was consistently higher using the WIR method (8.1 wt% for 2D and 8.7 wt% for 3D supports) compared to the MW method (7.5 wt% for 2D and 6.4 wt% for 3D supports). The lower Pt loadings obtained using the MW method, compared to the WIR method, may be attributed to the significantly shorter impregnation time. While the WIR process allows nearly 24 hours for metal incorporation, the MW method was completed within only 25 minutes, which may limit the extent of platinum deposition onto the support. In addition, platinum losses were observed during the catalyst filtration and washing steps which are discussed below.

Along with the main elements, other elements were also detected by XRF. Si content up to 6.7 wt% and Mg content around 1.5 wt% were detected in the case of using MoS_2 as the support. These elements are taken as the impurities of the support material originating from its preparation. Other elements including Ca, Fe, Cu, Pb and Al were detected in small amounts below 1 wt%.

To further validate the catalyst composition, SEM/EDS analysis was performed. EDS confirmed the presence of Pt NPs *via* a peak at approximately ~2.2 keV which is in line with previous literature.[42] In comparison with the XRF measurements, EDS showed slightly lower Pt contents, which was expected because EDS investigates a smaller, surface-localized volume than XRF. Even so, the EDS data were consistent with the XRF trends, reproducing the same relative differences in Pt loadings. Additional information obtained using SEM analysis is discussed below.

Inductively coupled plasma optical emission spectroscopy (ICP-OES)

During the catalyst preparation, a filtration step was used to separate the solid catalyst from the liquid phase. The resulting filtrate was analyzed by ICP-OES to determine whether any platinum (Pt) remained in solution. The analysis showed that some of the Pt remained dissolved, with a concentration of 1.21 mg L^{-1} (RSD 4.92%), indicating incomplete deposition of Pt onto the TMD support. This result explains the lower Pt content observed in the XRF analysis of several samples, confirming that not all Pt was successfully anchored and that some fraction remained in the impregnation solution. The ICP-OES data therefore corroborate the XRF findings. Notably, this issue was mainly observed for catalysts prepared *via* the microwave-assisted method, whereas catalysts synthesized by the incipient wetness method exhibited minimal platinum losses.

Atomic absorption spectrometry (AAS)

After filtration, the catalyst retained on the filter paper was rinsed three times with distilled water (3 × 10 mL) to remove any soluble residues. The combined washing solutions were analyzed by AAS to assess potential Pt loss during the washing step. The results confirmed that only a small amount of Pt was leached from the support with Pt concentrations in the washing water remaining below 0.7 mg L^{-1}, indicating that washing contributed only minimally to overall Pt losses.

When combining the Pt mass balance from all analytical methods, XRF (Pt anchored on the support), ICP-OES (Pt remaining in the impregnation solution), and AAS (Pt present in the washing water), the overall Pt recovery exceeds 90%. Considering the measurement uncertainties of all three techniques, the Pt mass balance can be regarded as closed, indicating that all Pt not immobilized on the support remains dissolved in the liquid phase.

Scanning electron microscopy (SEM)

The surface morphology of all the prepared catalysts was examined using scanning electron microscopy (SEM) equipped with a backscattered electron (BSE) detector. Representative SEM images of the Pt catalysts supported on bulk forms of TMDs are shown in Fig. 2 and in the SI (Fig. S1a–i). Some dark regions and bright particles are visible in certain images; however, it is difficult to determine whether these features correspond to Pt nanoparticles. No significant differences were observed between the catalysts prepared by the different methods or between the bulk and exfoliated

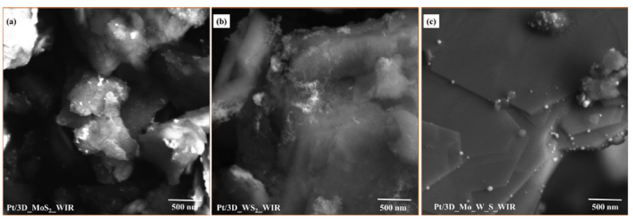

Fig. 2 SEM images of (a) Pt/3D-MoS_2-WIR, (b) Pt/3D-WS_2-WIR and (c) Pt/3D-Mo–W–S-WIR.

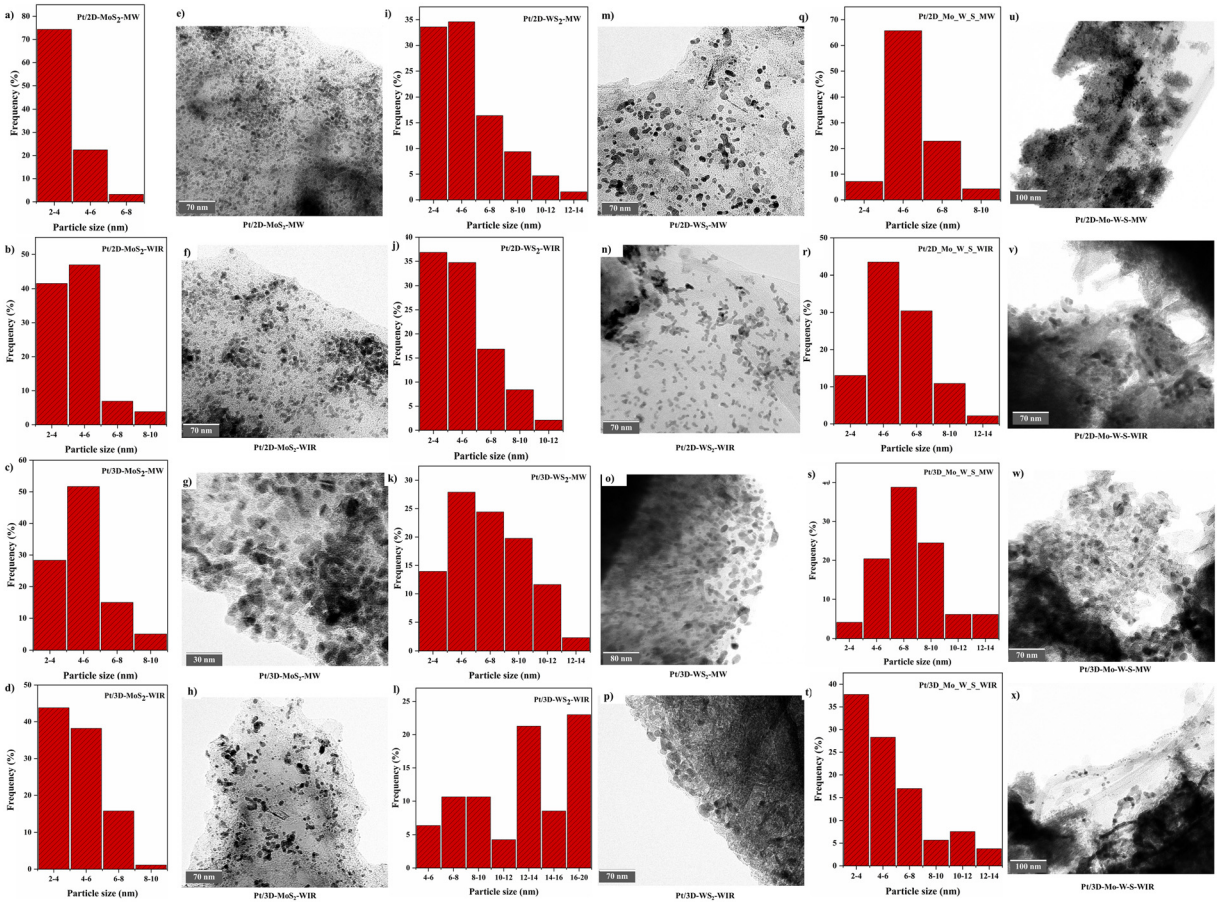

Fig. 3 Comparative TEM study: particle size distribution of MoS_2-based catalysts (a–d) and their corresponding TEM images (e–h), particle size distribution of WS_2-based catalysts (i–l) and their corresponding TEM images (m–p), particle size distribution of Mo–W–S-based catalysts (q–t) and their corresponding TEM images (u–x).

supports. Fig. 2(a–c) display the SEM images of Pt nanoparticles supported on pure bulk materials MoS_2 and WS_2 and their composite Mo–W–S synthesized *via* the WIR method.

Transmission electron microscopy (TEM)

TEM analysis was used for a more detailed study of the Pt NP morphology and size. The TEM images and Pt particle size distributions presented in Fig. 3 confirm the successful deposition of Pt nanoparticles on all TMD supports, appearing as dark, quasi-spherical domains uniformly dispersed across the support surface. Despite high Pt loadings (up to 9.2 wt%), no severe agglomeration or large cluster formation was observed.

MoS_2-supported catalysts shown in Fig. 3(a–d) exhibited the narrowest particle size distributions (2–10 nm). Pt/2D-MoS_2-MW contained the smallest particles, with ~70% in the 2–4 nm range, while other MoS_2 samples displayed ~80% between 2 and 6 nm, with minor populations up to 9 nm. All particles were predominantly spherical.

TEM analysis of WS_2-supported catalysts demonstrated in Fig. 3(i–l) revealed pronounced support effects. The exfoliated 2D variants (Pt/2D-WS_2-WIR and Pt/2D-WS_2-MW) contained predominantly particles ranging between 2 and 6 nm, with only small fractions extending to 8–12 nm. In contrast, bulk WS_2 contained a broader distribution of Pt NP sizes. The Pt/3D-WS_2-MW catalyst was enriched in the 4–8 nm range, whereas Pt/3D-WS_2-WIR shifted toward larger particles (12–20 nm). But it should be noted here that a much lower Pt loading was determined for the Pt/3D-WS_2-MW catalyst being only 1.2 wt%. These results further confirm our conclusion that Pt interacts less strongly with WS_2 than with MoS_2, leading to lower Pt loading efficiency and the formation of larger Pt NPs when WS_2 is used as the support. The TEM images of the Mo–W–S composite-based catalysts are presented in Fig. 3(q–t). Microwave-assisted synthesis yielded finer, more uniform dispersions than WIR. Pt/2D-Mo–W–S-MW was sharply centred at 4–6 nm (>70% population), while WIR-derived samples exhibited broader distributions (2–14 nm).

Overall, the use of exfoliated 2D supports and microwave-assisted synthesis promoted smaller, more homogeneously dispersed Pt NPs, whereas 3D supports and WIR methods led to broader distributions and partial agglomeration.

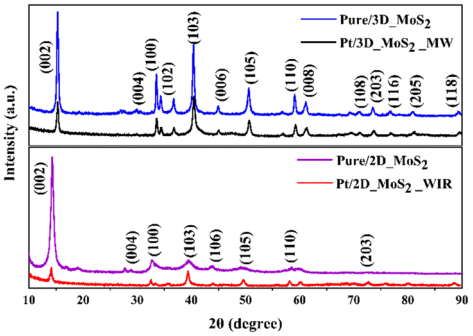

Fig. 4 XRD patterns of pure MoS_2 supports and MoS_2-based catalysts.

X-ray diffraction (XRD)

The crystalline structures of the prepared catalysts were investigated using X-ray diffraction (XRD). Fig. 4 compares the patterns of pristine 3D-MoS_2 and its 2D counterpart. Both exhibited sharp reflections characteristic of the hexagonal MoS_2 phase, with the dominant (002) peak at 14.4° 2θ (ICCD card No. 37-1492).[43,44] In the 2D-MoS_2 sample, the persistence of this (002) reflection together with the attenuation of secondary peaks confirms the formation of few-layer nanosheets with reduced *c*-axis stacking.

Catalyst diffractograms closely resembled those of their pristine MoS_2 supports. Notably, 2D-MoS_2-WIR displayed sharper peaks relative to pristine 2D-MoS_2, suggesting partial restacking of the material layers and improved long-range order, consistent with the structural rearrangements often observed upon impregnation. Importantly, no distinct Pt reflections were detected in any MoS_2-supported catalysts, indicating that Pt nanoparticles remained highly dispersed and below the XRD detection threshold. This observation aligns with previous reports, where even at ~8 wt% Pt loading, diffraction peaks were absent due to the nanoscale particle dimensions and uniform dispersion.[45]

Fig. 5 presents the XRD patterns of Pt-loaded catalysts supported on 3D-WS_2 and its 2D analogues. For bulk WS_2, intense reflections were observed at 14.2°, 28.6°, 32.6°, 33.4°, 39.6°, 44.0°, 49.6°, 58.2°, 60.0°, 60.3°, 66.7°, and 76.0° 2θ, corresponding to the (002), (004), (100), (101), (103), (006), (105), (110), (008), (112), (114), and (116) planes of the hexagonal WS_2 phase (JCPDS 00-08-0237).[46] In contrast, the 2D-WS_2 nanosheets exhibited only a single reflection at ~14.2° 2θ, indexed to the (002) plane, consistent with monolayered or few-layered structures reported in the literature.[47] Pt/3D-WS_2 catalysts retained the major features of the bulk support but exhibited two additional peaks at 23.9° and 35.8° 2θ (denoted in Fig. 5 by *), which are absent in pristine WS_2 and likely arise from partial oxidation during preparation. These are consistent with low-crystallinity WO_3, which typically exhibits a cluster of reflections at 23–24° 2θ (JCPDS 20-1324).[48,49] The appearance of WO_3-related peaks is attributed to partial oxidation of the WS_2 support during catalyst preparation. XRF analysis indicates a decrease in sulfur content after Pt deposition; specifically in the Pt/3D-WS_2-WIR catalyst, the sulfur content decreased to ~16 wt%, compared with ~24 wt% for the pristine support, and in the XRD results, this catalyst showed prominent appearance of the WO_3 peak. Sulfur depletion is consistent with the formation of S vacancies, which create under-coordinated W sites and increase the susceptibility of the material to oxidation. Consequently, these defect sites can promote partial conversion of the sulfide phase to WO_3, giving rise to the observed WO_3 signals.

In comparison with the pure supports, two additional weak peaks were observed in the pattern of Pt/3D-WS_2-WIR at 46.3° 2θ (200) and 67.8° 2θ (220), which correspond to metallic Pt nanoparticles (JCPDS 04-0802). This result is in good agreement with the TEM analysis, which indicated the presence of the largest Pt nanoparticles among all the prepared catalysts. For catalysts derived from 2D-WS_2 supports, partial restacking of nanosheets was evident, as weaker but discernible peaks appeared at the same positions as those of bulk WS_2. This phenomenon, commonly reported in the literature,[50–52] is attributed to solvent removal during drying, which enables van der Waals-driven reaggregation of exfoliated layers. As shown in Fig. 6, all Mo–W–S composites preserved the 2H-layered

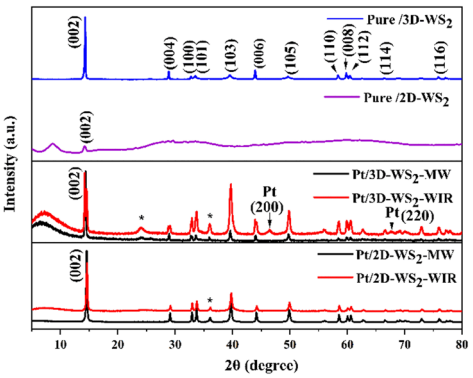

Fig. 5 XRD patterns of pure WS_2 supports and WS_2-based catalysts.

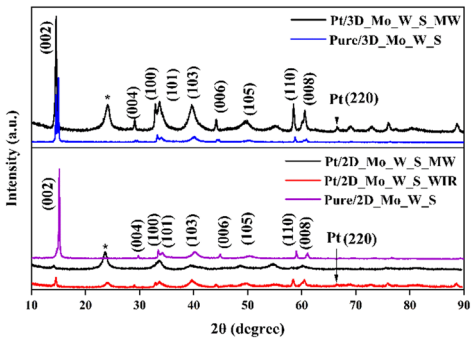

Fig. 6 XRD patterns of pure Mo–W–S supports and Mo–W–S-based catalysts.

structure, with reflections assignable to both MoS_2 and WS_2 phases. The peaks were generally broader and less intense than those of the pure phases, indicative of reduced crystallinity due to Mo/W lattice mixing. Bulk samples displayed sharper reflections, consistent with larger crystallites. In all cases, the (002) reflection near 14° 2θ remained prominent. Catalyst samples also exhibited additional peaks; in Pt/3D-Mo–W–S-MW, a peak marked (*) was observed, attributed to partial WS_2 oxidation, while a weak reflection at 67.5° 2θ corresponding to Pt(220) confirmed the presence of metallic Pt nanoparticles.

Nitrogen physisorption

The nitrogen physisorption method was used to calculate the BET surface areas of Pt-supported catalysts prepared on 3D-MoS_2, 3D-WS_2, and 3D-Mo–W–S supports using both the WIR and MW methods and the results are summarized in the SI (Table S2). There was significant effort to determine values for specific surface areas also for the 2D analogues of the tested supports; however, the method was developed for porous materials and therefore it gives unreproducible results for materials with only apparent porosity given by interlayer spacing. For the MoS_2-based catalysts, the surface areas were 27 $m^2\ g^{-1}$ (Pt/3D-MoS_2-WIR) and 21 $m^2\ g^{-1}$ (Pt/3D-MoS_2-MW), indicating that the surface areas remain relatively low and do not vary much between treatments. In contrast, the WS_2-supported catalysts showed the highest variation, with Pt/3D-WS_2-MW exhibiting a significantly larger surface area (58 $m^2\ g^{-1}$) compared to Pt/3D-WS_2-WIR (20 $m^2\ g^{-1}$). In the case of the Mo–W–S composite supports, the MW-prepared catalyst had a moderate surface area of 22 $m^2\ g^{-1}$, while the WIR-prepared catalyst displayed the lowest value (5 $m^2\ g^{-1}$). In particular, the MW method generally enhanced the surface area compared to WIR for WS_2 and the Mo–W–S composite, whereas the difference was less pronounced for MoS_2-based systems.

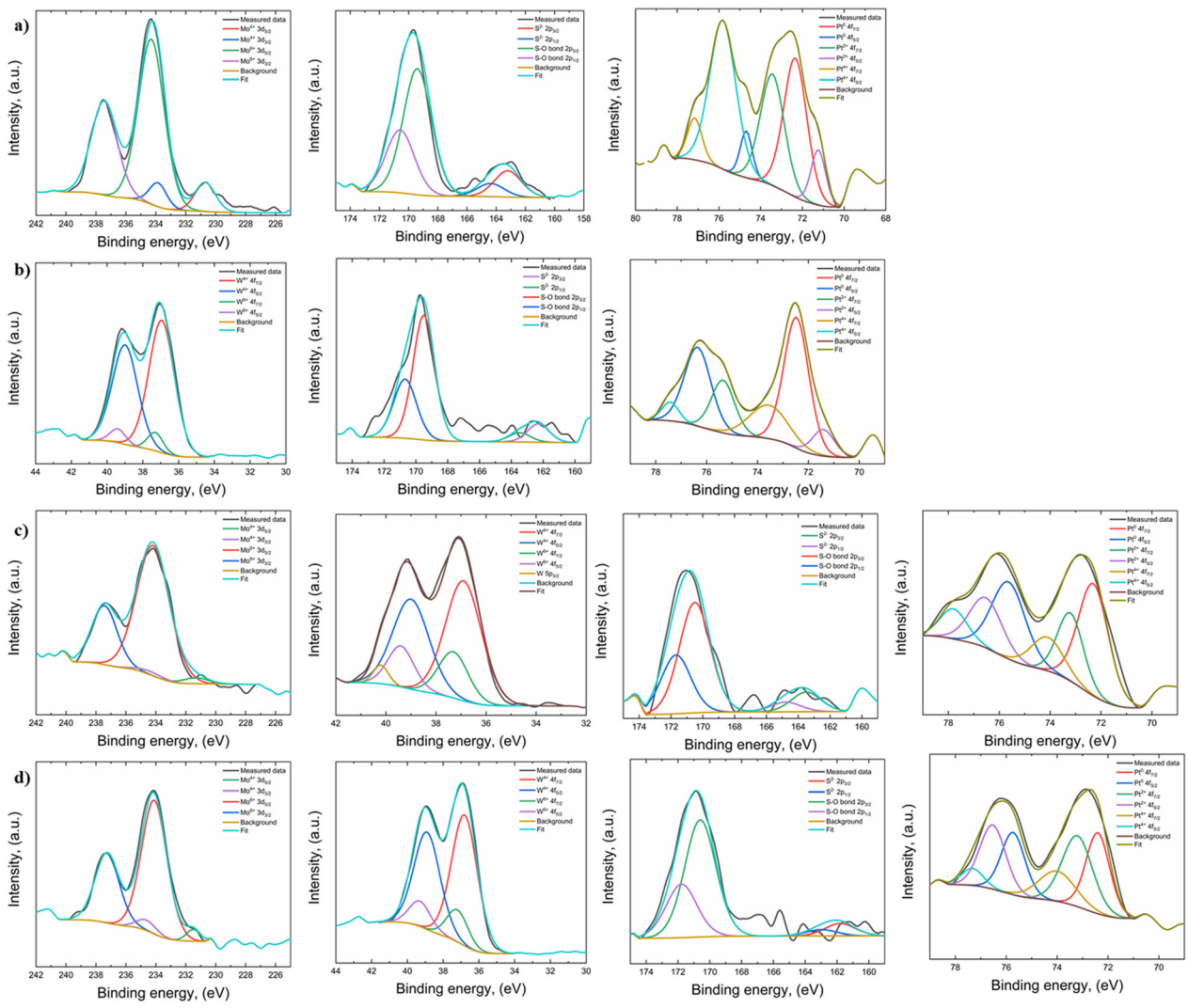

Fig. 7 XPS high-resolution Mo 3d and/or W 4f, S 2p and Pt 4f spectra of (a) Pt/3D-MoS_2-MW, (b) Pt/2D-WS_2-MW, (c) Pt/2D-Mo–W–S-MW and (d) Pt/3D-Mo–W–S-MW.

Photoelectron spectroscopy

High-resolution X-ray photoelectron spectroscopy (XPS) was conducted to elucidate the surface chemical states of Pt/3D-MoS_2-MW, Pt/2D-WS_2-MW, and Pt/Mo–W–S in both 2D and 3D architectures. For Pt/3D-MoS_2-MW, the Mo 3d spectrum is dominated by Mo^{6+} peaks located at ~234.5 eV ($3d_{5/2}$) and ~237.6 eV ($3d_{3/2}$), indicating pronounced surface oxidation of molybdenum (Fig. 7a). Minor contributions at ~230.8 and ~233.9 eV correspond to Mo^{4+}, suggesting that only a small fraction of Mo remains in the sulfide state. The S 2p spectrum is primarily composed of S–O components at ~169.5 eV ($2p_{3/2}$) and ~170.7 eV ($2p_{1/2}$), while weak doublets at ~163.3 and ~164.5 eV are assigned to sulfide (S^{2-}) species, confirming substantial sulfur oxidation. In the Pt 4f region, metallic Pt^0 appears at ~71.2 eV ($4f_{7/2}$) and ~74.5 eV ($4f_{5/2}$), whereas the dominant contribution arises from Pt^{2+} (~72.6 and ~75.9 eV), accompanied by weaker Pt^{4+} peaks (~74.2 and ~77.5 eV), indicating that Pt predominantly exists in an oxidized state.

For Pt/2-WS_2-MW, the W 4f spectrum shows dominant W^{4+} doublets at ~36.5 eV ($4f_{7/2}$) and ~38.6 eV ($4f_{7/2}$), confirming that tungsten largely retains its sulfide state (Fig. 7b). Minor W^{6+} features at ~37.3 and ~39.4 eV indicate limited surface oxidation. Similar to the Mo-based sample, the S 2p region is dominated by S–O species (~169.4 and ~170.6 eV), with minor sulfide contributions (~162.5 and ~163.7 eV). The Pt 4f spectrum is mainly composed of Pt^{2+} (~72.5 and ~75.8 eV), with smaller amounts of metallic Pt^0 (~71.1 and ~74.4 eV) and Pt^{4+} (~74.0 and ~77.2 eV).

For the mixed Pt/2D-Mo–W–S-MW system (Fig. 7c), the Mo 3d spectrum is again dominated by Mo^{6+} species with only weak Mo^{4+} contributions, indicating that Mo remains highly susceptible to surface oxidation. In contrast, the W 4f region exhibits predominantly W^{4+} with minor W^{6+} components, demonstrating that tungsten preserves the sulfide framework more effectively. The S 2p spectrum is largely composed of S–O signals with minor S^{2-} contributions, reflecting substantial surface sulfur oxidation. In this case, the Pt 4f region is dominated by metallic Pt^0, accompanied by minor Pt^{2+} and Pt^{4+} components, suggesting that Pt is primarily present in a reduced metallic state.

For the Pt/3D-Mo–W–S-MW architecture (Fig. 7d), the Mo 3d spectrum remains Mo^{6+}-rich with only trace Mo^{4+}, confirming extensive surface oxidation of Mo. The W 4f region is still dominated by W^{4+} with minor W^{6+} contributions, indicating preservation of tungsten in the sulfide state. The S 2p spectrum is mainly composed of S–O species with minor sulfide signals, consistent with partial surface oxidation. Notably, the Pt 4f spectrum shows comparable contributions from Pt^0 and Pt^{2+}, along with a minor Pt^{4+} fraction, indicating a higher proportion of interfacial or partially oxidized Pt species compared to the 2D mixed phase.

The XPS results show clear trends in surface chemistry: Mo-containing samples exhibit predominantly Mo^{6+} surface species, whereas W largely remains in the W^{4+} sulfide state. Sulfur is significantly oxidized at the surface in all materials, as indicated by dominant S–O signals. The Pt oxidation state varies with composition and architecture: Pt^{2+} dominates in Pt/MoS_2 and Pt/WS_2, metallic Pt^0 is prevalent in the 2D Pt/2D-Mo–W–S system, and a mixed Pt^0/Pt^{2+} state appears in the 3D mixed catalyst. These trends suggest that W incorporation stabilizes the sulfide framework and promotes metallic Pt, while the 3D architecture enhances metal–support interactions and facilitates partial Pt oxidation or interfacial charge redistribution.

Importantly, XRD detected WO_3 formation only in samples that did not undergo XPS analysis (*e.g.*, Pt/3D-WS_2). This indicates that bulk oxidation of WS_2 to WO_3 occurred during storage or handling, but was not present in the specific samples analyzed by XPS. Since XPS probes only the top ~5 nm, it is highly sensitive to surface oxidation (S–O, Mo^{6+}), whereas XRD detects bulk crystalline phases. The absence of MoO_3 reflections in the MoS_2-based samples confirms that MoS_2 retained its hexagonal structure, with no

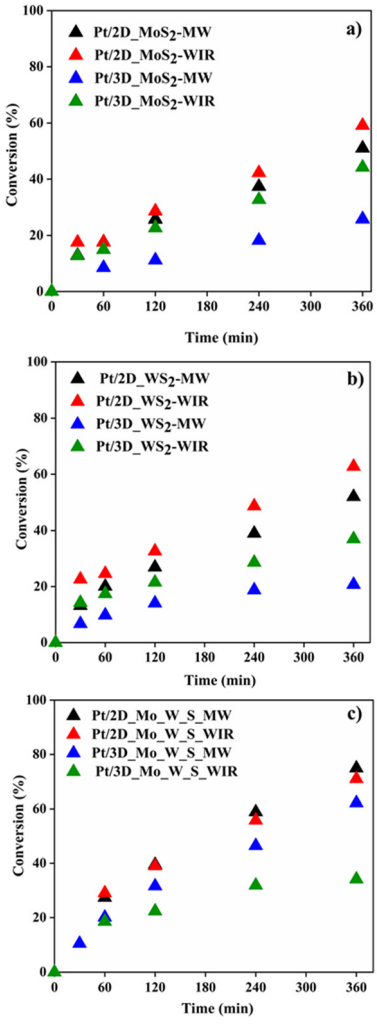

Fig. 8 CAL conversion as a function time using different catalytic systems: (a) Pt/MoS_2, (b) Pt/WS_2 and (c) Pt/Mo–W–S.

detectable bulk oxidation. Together, these results show that surface oxidation is widespread and captured by XPS, while bulk oxidation (WO_3 formation) is sample-dependent and only observed by XRD in materials not analyzed by XPS. The two techniques therefore provide complementary information rather than contradictory results.

Catalytic testing: cinnamaldehyde hydrogenation

Catalyst activities: conversion of cinnamaldehyde. The catalytic performance of the prepared materials evaluated in cinnamaldehyde (CAL) hydrogenation is summarized in Fig. 8 as a function of conversion with reaction time. In all cases, conversion increased monotonically with time, though pronounced activity differences were evident across catalytic systems. The nature of the support exerted the dominant influence, with Mo–W–S consistently outperforming both MoS_2 and WS_2. Composite-supported catalysts achieved the highest overall conversions (~70–75% within 360 min), while bulk supports were systematically less active than their 2D analogues. Fig. 8a presents the results obtained using MoS_2-supported catalysts. Pt/2D-MoS_2-WIR exhibited the highest activity, reaching ~18% conversion at 60 min and ~59% at 360 min, clearly surpassing bulk-MoS_2-based systems. This enhancement is attributed to improved Pt dispersion and greater accessibility of active sites in the 2D structure. A similar trend was observed for WS_2-supported catalysts (presented in Fig. 8b), albeit with higher overall conversions. Pt/2D-WS_2-WIR displayed rapid initial activity (~23% at 60 min) and attained ~63% conversion at 360 min, while Pt/2D-WS_2-MW reached ~52% at the same time. By contrast, bulk WS_2 catalysts remained significantly less active, with maximum conversions below 40% after 360 min. Fig. 8c demonstrates CAL conversions achieved using Mo–W–S composite-based catalysts. These catalysts exhibited the most promising catalytic behaviour. Pt/2D-Mo–W–S-MW achieved ~29% conversion at 60 min and ~75% at 360 min, closely followed by Pt/2D-Mo–W–S-WIR (~70% at 360 min). Even the bulk composites outperformed bulk MoS_2 and WS_2, underscoring the intrinsic advantage of the Mo–W composite.

To gain insight into the reaction progress, the reaction rates and turn over frequencies were determined for all tested catalysts and Table 3 shows a detailed comparison of these values. The rates were calculated with consideration of the Pt NP loading (XRF data) and mass of the catalyst used in the reaction. Meanwhile in TOF calculation, Pt dispersion on the surface was used, which was calculated using the average particle size obtained from TEM analysis. The initial reaction rates were derived from CAL concentrations measured between 0 and 30 min. Although this time interval is relatively long, the recorded conversions remained below 25%, indicating that the reactions proceeded within the initial kinetic regime. Overall, the initial reaction rates were consistently higher than the rates observed at higher reaction times, reflecting a decline in activity as the reaction progressed.

Among the MoS_2-based catalysts, the Pt/2D-MoS_2-WIR catalyst exhibited the highest initial as well as final reaction rates. Also, this catalytic system showed the highest TOF and showed good alignment with the obtained rate of reactions. These findings are consistent with the conversion profiles presented in Fig. 8.

For the WS_2-based catalysts, the reaction rates normalized to catalyst mass demonstrate that catalysts with lower Pt loadings exhibited the highest initial reaction rates. For instance, 3D-WS_2-MW, with the lowest Pt loading of 1.2 wt%, displayed the highest initial rate among all the tested catalysts being 14.1×10^{-2} mmol min^{-1} mg_{Pt}^{-1}. A similar trend was observed for the 2D-WS_2-based catalysts. The TOF data were also consistent with these findings. This behaviour is attributed to the fact that, at lower loadings, a larger fraction of Pt nanoparticles actively participated in the catalytic process. Similarly in the Mo–W–W-based system, the catalyst containing a lower Pt loading of 6.4 wt% exhibited a higher TOF of 3.7×10^{-1} s^{-1} and the highest final reaction rates.

The subsequent decline in reaction rates suggests either partial catalyst deactivation or the saturation of active sites.

Table 3 Rate of reactions achieved over tested catalysts

Catalyst	CAL conversion (%)	XRF Pt loading (wt%)	r_0 (mmol min^{-1} mg_{Pt}^{-1}) ($\times 10^{-2}$)	r_t (mmol min^{-1} mg_{Pt}^{-1}) ($\times 10^{-2}$)	Average Pt size from TEM (nm)	TOF (s^{-1}) ($\times 10^{-1}$)
Pt/2D-MoS_2-MW	51	10.5	3.5	0.9	3.9	1.2
Pt/2D-MoS_2-WIR	59	10.5	4.9	1.1	4.5	1.6
Pt/3D-MoS_2-MW	26	10.0	1.4[a]	0.5	4.9	0.8
Pt/3D-MoS_2-WIR	44	10.5	4.6	0.8	3.6	0.7
Pt/2D-WS_2-MW	52	3.6	9.2	2.5	5.5	4.3
Pt/2D-WS_2-WIR	63	9.0	6.2	1.0	5.1	1.8
Pt/3D-WS_2-MW	21	1.2	14.1	2.7	6.7	5.9
Pt/3D-WS_2-WIR	37	8.7	4.2	0.6	14.4	2.7
Pt/2D-Mo–W–S-MW	75	7.5	4.4[a]	1.5	5.4	2.7
Pt/2D-Mo–W–S-WIR	71	8.1	4.6[a]	1.3	5.9	2.8
Pt/3D-Mo–W–S-MW	62	6.4	4.1	1.8	7.7	3.7
Pt/3D-Mo–W–S-WIR	34	8.7	2.7[a]	0.5	5.2	0.5

r_0 = initial reaction rates (0–30 min), r_t = reaction rate between 30 and 360 min; reaction conditions (CAL, isopropyl alcohol, 80 °C, 1 MPa, 6 h).
[a] 60 min.

However, regardless of the loading, catalytic activity was strongly limited at longer reaction times. Overall, among all the studied catalysts, higher rates of reaction were observed among the 2D-supported catalysts compared to the bulk supports. It is obvious that exfoliated supports exhibit higher exposed surface and defect sites which enhance the probability of reactant adsorption and reaction compared to bulk, less defective surfaces.[53]

Selectivities toward hydrogenation and side-products. The selectivities toward cinnamyl alcohol (COL), hydrocinnamaldehyde (HCAL), and hydrocinnamyl alcohol (HCOL) obtained over Pt-supported catalysts were evaluated as a function of CAL conversion. Next to the listed products of hydrogenation, one side-product was detected using GC. GC-MS analysis confirmed the side-product as 3-isopropoxy-propan-1-yl benzene (named "ether"), formed *via* reductive etherification of CAL with isopropanol under reaction conditions, consistent with previous reports.[40]

COL, the product of carbonyl group hydrogenation, was the main product obtained using all the tested catalysts and its selectivity increased with increasing CAL conversion in all presented hydrogenation experiments. HCAL, an aldehyde with a hydrogenated olefinic double bond, was produced in significantly smaller amounts, with selectivities toward HCAL remaining below 10%. Additionally, the formation of HCOL, the product of hydrogenation of both olefinic and carbonyl double bonds, was minimal (≤5%) and absent in the bulk-MW catalyst. At early stages, COL and ether were formed competitively, but COL became dominant as the reaction progressed. Fig. 9(a–d) present selectivities obtained over MoS_2-supported catalysts. COL selectivities up to 60% were achieved using all MoS_2-based catalysts. Results obtained over WS_2-supported catalysts presented in Fig. 9(e–h) demonstrated COL as the dominant product with the highest selectivity (54%) observed for Pt/2D-WS_2-WIR. Ether was consistently formed as a side-product, with selectivity reaching 28% in 2D-based catalysts and up to 43% in bulk catalysts at low conversions before decreasing as COL formation increased. Other hydrogenated products HCAL and HCOL remained below 10%. In Pt/3D-WS_2-MW, the COL selectivity was poor (<32%), with ether as the main product and HCOL reaching 20% at a low conversion level.

As was observed in XRD, additional diffraction peaks corresponding to WO_3 were observed only for the bulk-

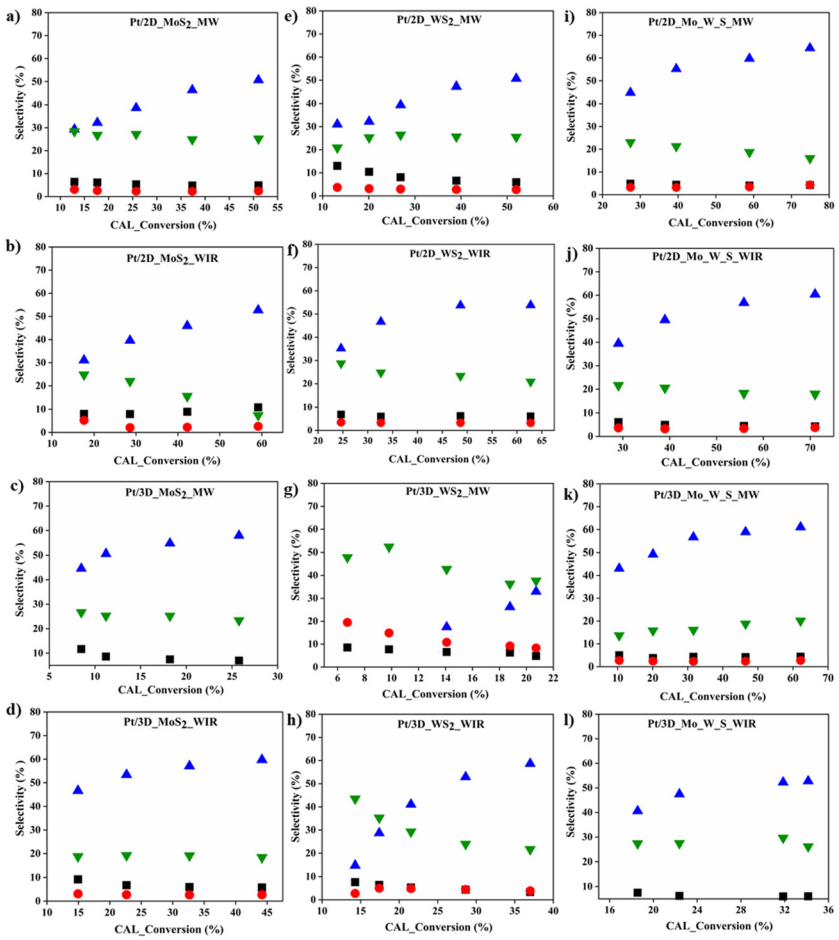

Fig. 9 Selectivities toward CAL hydrogenated products (HCAL, HCOL, and COL) as a function of CAL conversion obtained using the prepared catalysts: (a–d) MoS_2-based catalysts, (e–h) WS_2-based catalysts and (i–l) Mo–W–S-based catalysts.

supported catalyst, whereas they are absent for the 2D-supported catalyst. Notably, the bulk-supported catalyst also exhibits a higher ether selectivity compared with the 2D-supported catalyst. Since the ether product is primarily associated with the solvent-derived pathway, these observations suggest that the WO_3 phases present in the bulk-supported catalyst facilitate ether formation, thereby enhancing the observed selectivity.

For the Mo–W–S-supported catalysts (Fig. 9(i–l)), COL was the dominant product, with selectivity increasing as conversion proceeded. The highest COL selectivity (64.3%) was obtained for the 2D-MW catalyst. Across all composites, the COL selectivity exceeded 40%. At low conversions, ether was formed competitively but remained below 23%, except for the bulk-WIR catalyst, which reached 30% and showed no HCOL formation. HCAL and HCOL selectivities remained consistently low (<8%) and their formation was rather constant during the whole reaction time. The Mo–W–S system particularly in the 2D nanosheet form (MW or WIR) achieved the best balance of high activity and high COL selectivity.

Additionally, product selectivities toward the primary hydrogenation products COL, HCAL and HCOL as well as by-product ether were determined at 10% and 30% CAL conversion levels for all the catalysts, as detailed in Table 4. Selectivities toward minor, unidentified by-products formed in small amounts are also reported to provide a complete picture of the product distribution under the given reaction conditions. The yields of hydrogenation products were also calculated as a function of time and the obtained results are shown in SI S4.

As discussed above, COL selectivities increased with increasing CAL conversion and the highest COL selectivities at the 30% conversion level exceeded 50% using all 3D-based supports independent of their chemical composition. The final CAL conversions, COL selectivities and COL yields obtained within 360 minutes of the reaction are described in Table 5. Among all, Pt/2D-Mo–W–S-MW showed the best results, with the highest CAL conversion (75%), COL selectivity (64%), and COL yield (48%).

Its counterpart prepared by conventional impregnation, Pt/2D-Mo–W–S-WIR, also performed well (71% CAL conversion, 61% COL selectivity, and 43% COL yield). In contrast, bulk (3D) catalysts generally exhibited lower activity and yields, confirming that 2D supports outperform 3D forms in the catalytic activity.

However, higher selectivities toward COL (at the 30% conversion level) are achieved using the bulk forms of supports but in combination with lower achieved CAL conversions, and the final COL yields are lower. Additionally, Mo–W composite supports consistently outperformed pure MoS_2 and WS_2, highlighting the advantage of the combined composition and 2D morphology for both activity and selectivity.

To further verify the possible reason for formation of ether, two additional control reactions were performed under identical reaction conditions, one using the pure MoS_2 support without Pt loading and the other employing a commercial Pt/Al_2O_3 catalyst. In the MoS_2-based system (without Pt), a CAL conversion of 6% was observed. The product distribution showed 27% selectivity toward HCAL, 4.7% toward HCOL, 38% selectivity toward ether, and 31% selectivity toward additional side-products. When the reaction was carried out using commercial 5% Pt/Al_2O_3, it resulted in 16% conversion with 38% selectivity toward HCAL, 25% toward COL, and 5% toward HCOL. The ether selectivity reached 18%, while additional side-product selectivity was 15%. The formation of ether in both catalytic systems indicates that ether production is not exclusively associated with a specific support material, nor can it be attributed solely to the acidity of the support. Instead, these findings suggest that solvent

Table 4 Selectivities toward COL, HCAL and HCOL at 10% and 30% CAL conversion levels

	Selectivity at 10%/30% conversion of CAL (%)											
	COL		HCAL		HCOL		Ether		Others		Sum of H_2 products	
Catalyst	10%	30%	10%	30%	10%	30%	10%	30%	10%	30%	10%	30%
Pt/2D-MoS_2-MW	29.3	38.6[a]	6.4	5.3[a]	3.1	2.3[a]	28.4	27.2[a]	32.8	26.6[a]	38.8	46.2[a]
Pt/2D-MoS_2-WIR	31.0[c]	39.6[d]	8.0[c]	8.0[d]	5.2[c]	2.1[d]	24.8[c]	22.0[d]	31.0[c]	28.3[d]	44.2[c]	49.7[d]
Pt/3D-MoS_2-MW	**50.5**	**57.9**[a]	8.6	7.0[a]	0	0	25.2	23.4[a]	15.7	11.7[a]	59.1	64.9[a]
Pt/3D-MoS_2-WIR	46.6[g]	**57.0**	9.2[g]	5.9	3.1[g]	2.6	18.7[g]	19.1	22.4[g]	15.4	55.8[g]	65.5
Pt/2D-WS_2-MW	31.0	39.3[d]	13.0	8[d]	3.7	3[d]	21	26.4[d]	31.3	23.3[d]	47.7	50.3[d]
Pt/2D-WS_2-WIR	0[e]	46.6	9.8[e]	6.1	0[e]	3.3	49[e]	24.7	41.2[e]	19.3	9.8[e]	56.0
Pt/3D-WS_2-MW	0	33[b]	7.7	4.8[b]	14.9	8.3[b]	52.3	37.6[b]	25.1	16.3[b]	22.6	46.1[b]
Pt/3D-WS_2-WIR	14.8[f]	53.0[e]	7.6[f]	4.4[e]	2.7[f]	4.4[e]	43[f]	24[e]	31.8[f]	14.2[e]	25.1[f]	61.8[e]
Pt/2D-Mo–W–S-MW	—	44.9[e]	—	4.8[e]	—	3.3[e]	—	23[e]	—	24[e]	—	53[e]
Pt/2D-Mo–W–S-WIR	—	39.4	—	6	—	3.6	—	21.6	—	29.4	—	49
Pt/3D-Mo–W–S-MW	43.0	**56.6**	5.0	4.3	2.7	2.3	13.7	16.1	35.6	20.7	50.7	63.2
Pt/3D-Mo–W–S-WIR	—	**52.2**	—	6.0	—	0	—	29.6	—	12.2	—	58.2

(—) = not recorded (lowest recorded conversion ≥20%). [a] 25% conversion. [b] 20% conversion. [c] 17% conversion. [d] 28% conversion. [e] 22% conversion. [f] 14.5% conversion. [g] 15% conversion.

Table 5 Hydrogenation results obtained at 360 min

	Results of CAL hydrogenation at 360 min		
Catalyst	CAL conversion (%)	COL selectivity (%)	COL yield (%)
Pt/2D-MoS_2-MW	51	51	26
Pt/2D-MoS_2-WIR	59	53	31
Pt/3D-MoS_2-MW	26	58	15
Pt/3D-MoS_2-WIR	44	60	26
Pt/2D-WS_2-MW	52	51	26
Pt/2D-WS_2-WIR	63	54	34
Pt/3D-WS_2-MW	21	33	7
Pt/3D-WS_2-WIR	37	59	22
Pt/2D-Mo–W–S-MW	**75**	**64**	**48**
Pt/2D-Mo–W–S-WIR	**71**	**61**	**43**
Pt/3D-Mo–W–S-MW	62	61	38
Pt/3D-Mo–W–S-WIR	34	53	18

chemistry played a role in ether formation. As discussed previously, this behavior is most likely related to the participation of isopropyl alcohol in a reductive etherification pathway.

Conclusions

Pt-based hydrogenation catalysts supported on bulk TMDs (MoS_2, WS_2, and Mo–W–S) and their 2D counterparts were synthesized using microwave-assisted and wet impregnation methods, and their performance in cinnamaldehyde (CAL) hydrogenation was evaluated in relation to their physicochemical properties, with particular emphasis on the support morphology (2D *vs.* bulk) and preparation method.

Comprehensive characterization was carried out using SEM/EDS, TEM, XRF, XRD, and BET analyses. SEM/EDS confirmed successful Pt deposition, with most catalysts achieving loadings close to the targeted 9 wt%, which was validated by XRF. Lower Pt loadings were detected only when WS_2 was used as the support in combination of the MW-assisted impregnation method. These results suggest a weaker Pt–WS_2 interaction compared to Pt–MoS_2. Metal losses were clearly observed during the filtration and washing steps. In the case of the microwave-assisted synthesis method, insufficient anchoring of the active metal onto the support surface was evident. This was confirmed by ICP-OES analysis of the filtrate and AAS analysis of the washing solutions, both of which detected measurable concentrations of Pt. These results demonstrate that the portion of platinum not effectively anchored on the support remained dissolved in the impregnation solution, thereby leading to lower Pt loadings determined by XRF compared to the targeted values.

The 2D catalysts favored finer dispersion, with most particles in the 2–6 nm range, while the 3D supports showed broader particle size distributions. Microwave-assisted synthesis produced smaller and more uniform nanoparticles compared to wet impregnation, particularly in Mo–W–S systems. In general, smaller and more uniformly distributed nanoparticles correlated with superior catalytic activity.

XRD analysis verified the hexagonal crystal phases of MoS_2 and WS_2, with 2D forms showing reduced secondary peaks characteristic of few-layer structures. Composite Mo–W–S exhibited broader and less intense reflections, consistent with reduced crystallinity caused by Mo/W mixing. Weak Pt peaks were occasionally detected, reflecting highly dispersed nanoscale Pt particles. Partial oxidation and restacking effects were observed in some cases, particularly in 2D WS_2, likely due to solvent removal during drying, which induced nanosheet collapse.

XPS reveals extensive surface oxidation of Mo and S, partial oxidation of Pt depending on the architecture, and greater sulfide stability in W-containing systems.

A strong correlation was observed between the surface area, XRD patterns, and CAL conversion for Mo–W–S supported catalysts. Pt/2D-Mo–W–S-WIR exhibited the highest achieved CAL conversion being 75%, with XRD features showing broader, less intense peaks indicative of increased interlayer spacing and enhanced Pt dispersion. However, surface area alone was insufficient, as adequate Pt loading was also essential, and insufficient metal content resulted in reduced activity despite high surface areas.

Catalytic evaluation confirmed that performance in CAL hydrogenation was predominantly governed by the support type and size distribution of Pt nanoparticles. The Mo–W–S composite, particularly in the 2D form, consistently outperformed MoS_2 and WS_2, delivering both the highest activity and the best selectivity toward cinnamyl alcohol (COL). Pt/2D-MoS_2-WIR and Pt/2D-WS_2-WIR outperformed their bulk counterparts, but the Mo–W composite nanosheets exhibited superior conversions and selectivity overall. Ether formed *via* the reductive etherification mechanism was detected as a competitive side-product at low conversions, especially using bulk catalysts, while HCAL and HCOL remained minor products. Across all systems, Pt-supported TMD catalysts favored selective hydrogenation of the carbonyl (C═O) group over the olefinic (C═C) bond, leading to high COL selectivity. This selectivity was attributed to the ability of well-dispersed Pt on engineered TMD supports to promote C═O chemisorption and activation. The preparation method had only a minor influence compared to the decisive role of support composition and dimensionality.

The most effective catalyst was Pt supported on 2D-Mo–W–S synthesized by the microwave-assisted impregnation method, which achieved 75% CAL conversion after 360 minutes, along with 64.3% selectivity to COL and a 48% yield. COL selectivity increased progressively with conversion. These findings highlight the strong potential of TMD-based supports, particularly the Mo–W composite in the 2D nanosheet form, for the design of efficient catalysts in selective CAL hydrogenation, with 2D structures consistently outperforming their bulk counterparts.

Author contributions

Conceptualization: M. P. and M. V.; methodology: M. P. and M. V.; validation: A. S., M. P., and M. V.; formal analysis: A. S., M. P., I. D., L. K. and M. V.; investigation: A. S., B. S., M. P., I. D., J. L., and L. K.; resources: J. L.; data curation: A. S., M. P., M. V. and I. D.; writing – original draft preparation: A. S., M. P. and M. V.; writing – review and editing: A. S. and M. P.; visualization: A. S., M. P. and M. V.; supervision: M. P. and M. V.; funding acquisition: M. P. and M. V. All authors have read and agreed to the published version of the manuscript.

Conflicts of interest

The authors declare no conflicts of interest.

Data availability

The data supporting this article have been included as part of the supplementary information (SI).

Supplementary information: S1: SEM images of (a–d) MoS_2-based catalysts, (e–h) WS_2-based catalysts and (i–l) Mo–W–S-based catalysts; S2: BET surface area comparison for Pt supported catalysts on bulk MoS_2, WS_2, and Mo–W–S; S3: XPS survey spectra of Pt/3D-MoS_2-MW, Pt/2D-WS_2-MW, Pt/2D-Mo–W–S-MW and Pt/3D-Mo–W–S-MW; S4: yield of hydrogenation products as a function of time. See DOI: https://doi.org/10.1039/d5cy01520k.

Raw data for this article, including SEM and TEM images, EDS maps, and XRF and XRD data are available at Zenodo under this DOI: https://doi.org/10.5281/zenodo.17886350.

Acknowledgements

This research was supported by the institutional support Dagmar Procházková Fund provided by the University of Chemistry and Technology in Prague and by the Czech Science Foundation (GACR No. 23-08083M).

Notes and references

1 L. Li, Z.-F. Jiao, J.-X. Zhao, D. Yao, X. Li and X.-Y. Guo, *J. Catal.*, 2023, **425**, 314–321.
2 L. Zhong, X. Liao, H. Cui, J. Huang, H. Luo, Y. Lv and P. Liu, *ACS Catal.*, 2024, **14**, 15799–15810.
3 X. Wang, X. Liang, P. Geng and Q. Li, *ACS Catal.*, 2020, **10**, 2395–2412.
4 L. Yue, D. Sun, I. Mahmood Khan, X. Liu, Q. Jiang and W. Xia, *Food Chem.*, 2020, **309**, 125513.
5 H. Liu, Q. Mei, S. Li, Y. Yang, Y. Wang, H. Liu, L. Zheng, P. An, J. Zhang and B. Han, *Chem. Commun.*, 2018, **54**, 908–911.
6 K. Nuithitikul and M. Winterbottom, in *Chemical Engineering Science*, 2004, vol. 59, pp. 5439–5447.
7 S. Jiménez, J. A. López, M. A. Ciriano, C. Tejel, A. Martínez and R. A. Sánchez-Delgado, *Organometallics*, 2009, **28**, 3193–3202.
8 S. Padmanaban, Y. Lee and S. Yoon, *J. Ind. Eng. Chem.*, 2021, **94**, 361–367.
9 M. Zhang, Y. Sun, X. Zhou, K. Yang, L. Sun, C. Qi and M. Zhang, *Chem. Eng. J.*, 2024, **479**, 147595.
10 Q. Lu, H. Wang, J. Sun, X.-Z. Wei, Q. Zhang, X. Zhang, L. Chen, J. Liu, Y. Chen and L. Ma, *Microporous Mesoporous Mater.*, 2024, **367**, 112979.
11 L. Wang, Y. Ma, H. Li, W. Luo and J. Liu, *J. Catal.*, 2024, **431**, 115391.
12 A. J. Marchi, D. A. Gordo, A. F. Trasarti and C. R. Apesteguía, *Appl. Catal., A*, 2003, **249**, 53–67.
13 F. Tian, M. Zhang, X. Zhang, X. Chen, J. Wang, Y. Zhang, C. Meng and C. Liang, *J. Mater. Sci.*, 2022, **57**, 3168–3182.
14 X. Gao, Y. Ma, Y. Ruan, W. Zhang, S. Zhang, W. Xiong, D. Tian, S. Yang, P. Fan, Y. Yang and Y. Dai, *Mol. Catal.*, 2024, **559**, 114096.
15 H. Shi, Y. Xu, T. Su, X. Luo, X. Xie, Z. Qin and H. Ji, *Catal. Sci. Technol.*, 2024, **14**, 1181–1190.
16 T. Yuan, D. Liu, Y. Pan, X. Pu, Y. Xia, J. Wang and W. Xiong, *Catal. Lett.*, 2019, **149**, 851–859.
17 X. Yuan, J. Zheng, Q. Zhang, S. Li, Y. Yang and J. Gong, *AIChE J.*, 2014, **60**, 3300–3311.
18 S. S. Mohire and G. D. Yadav, *Ind. Eng. Chem. Res.*, 2018, **57**, 9083–9093.
19 S. Chen, L. Meng, B. Chen, W. Chen, X. Duan, X. Huang, B. Zhang, H. Fu and Y. Wan, *ACS Catal.*, 2017, **7**, 2074–2087.
20 A. S. Nagpure, L. Gurrala, P. Gogoi and S. V. Chilukuri, *RSC Adv.*, 2016, **6**, 44333–44340.
21 Z. Xu, C. Duong-Viet, Y. Liu, W. Baaziz, B. Li, L. Nguyen-Dinh, O. Ersen and C. Pham-Huu, *Appl. Catal., B*, 2019, **244**, 128–139.
22 H. Ma, T. Yu, X. Pan and X. Bao, *Chin. J. Catal.*, 2017, **38**, 1315–1321.
23 Y. Zhang, S. Zhang, X. Pan, M. Bao, J. Huang and W. Shen, *Catal. Lett.*, 2017, **147**, 102–109.
24 C. Li, C. Ke, R. Han, G. Fan, L. Yang and F. Li, *Mol. Catal.*, 2018, **455**, 78–87.
25 Y. Zhang, C. Chen, W. Gong, J. Song, Y. Su, H. Zhang, G. Wang and H. Zhao, *RSC Adv.*, 2017, **7**, 21107–21113.
26 Y. Xue, H. Xin, W. Xie, P. Wu and X. Li, *Chem. Commun.*, 2019, **55**, 3363–3366.
27 D. Hu, W. Fan, Z. Liu and L. Li, *ChemCatChem*, 2018, **10**, 779–788.
28 Z. Tian, Q. Li, J. Hou, Y. Li and S. Ai, *Catal. Sci. Technol.*, 2016, **6**, 703–707.
29 S. Wei, Y. Zhao, G. Fan, L. Yang and F. Li, *Chem. Eng. J.*, 2017, **322**, 234–245.
30 L. Wang, Y. Ma, H. Li, W. Luo and J. Liu, *J. Catal.*, 2024, **431**, 115391.
31 K. N. Patil, P. Manikanta, P. M. Srinivasappa, A. H. Jadhav and B. M. Nagaraja, *J. Environ. Chem. Eng.*, 2023, **11**, 109168.
32 Y. Qu, H. Pan and C. T. Kwok, *Sci. Rep.*, 2016, **6**, 34186.
33 M. Pitínová, A. Krnáčová, A. Shafiq, I. Danylo, L. Koláčný and M. Veselý, *Catal. Today*, 2025, **460**, 115473.
34 G. Wang, X.-L. Jiang, Y.-F. Jiang, Y.-G. Wang and J. Li, *ACS Catal.*, 2023, **13**, 8413–8422.

35 H. Li, L. Wang, Y. Dai, Z. Pu, Z. Lao, Y. Chen, M. Wang, X. Zheng, J. Zhu, W. Zhang, R. Si, C. Ma and J. Zeng, *Nat. Nanotechnol.*, 2018, **13**, 411–417.
36 F. Shi, W. Wu, J. Chen and Q. Xu, *Chem. Commun.*, 2021, **57**, 7011–7014.
37 I. Danylo, L. Koláčný, K. Kissíková, T. Hartman, M. Pitínová, J. Šturala, Z. Sofer and M. Veselý, *Nanoscale Adv.*, 2025, **7**, 2021–2031.
38 Y.-J. Li, K. Dong, X.-K. Ma, J. Shi, J.-W. Fu, G.-W. Chu, H.-K. Zou and B.-C. Sun, *Sep. Purif. Technol.*, 2023, **315**, 123631.
39 Z. Sofer, D. Sedmidubský, J. Luxa, D. Bouša, Š. Huber, P. Lazar, M. Veselý and M. Pumera, *Chem. – Eur. J.*, 2017, **23**, 10177–10186.
40 M. Pitínová, I. Danylo, A. Shafiq, T. Hartman, M. Khover, B. Sevemez, L. Koláčný and M. Veselý, *Catalysts*, 2025, **15**, 470.
41 Y. Bai, N. Cherkasov, S. Huband, D. Walker, R. Walton and E. Rebrov, *Catalysts*, 2018, **8**, 58.
42 K. ur Rehman, M. Gouda, U. Zaman, K. Tahir, S. U. Khan, S. Saeed, E. Khojah, A. El-Beltagy, A. A. Zaky, M. Naeem, M. I. Khan and N. S. Khattak, *Nanomaterials*, 2022, **12**, 1079.
43 Y. Qi, N. Wang, Q. Xu, H. Li, P. Zhou, X. Lu and G. Zhao, *Chem. Commun.*, 2015, **51**, 6726–6729.
44 S. Arun, C. Arul, S. Mithin Kumar, U. Venkat Kiran and S. Mayavan, *ChemistrySelect*, 2020, **5**, 2469–2475.
45 X. Li, J. Pang, W. Luo, Y. Zhao, X. Pan and M. Zheng, *Catal. Lett.*, 2021, **151**, 2734–2747.
46 A. Neog and R. Biswas, *Mater. Res. Bull.*, 2021, **144**, 111471.
47 Y. Q. Qin, Y. Q. Peng, W. F. Yang, Y. Wang, J. W. Cui and Y. Zhang, *IOP Conf. Ser.: Mater. Sci. Eng.*, 2020, **770**, 012079.
48 G. Shen, Y. Yan, J. Tan and K. Hong, *J. Mater. Sci.*, 2022, **57**, 18819–18826.
49 G. Li, Y. Wang, J. Bi, X. Huang, Y. Mao, L. Luo and H. Hao, *Nanomaterials*, 2020, **10**, 278.
50 X. Zhang, J. Wang, H. Xu, H. Tan and X. Ye, *Nanomaterials*, 2019, **9**, 840.
51 M. Bandpey and D. P. J. Barz, *Nanoscale*, 2024, **16**, 15078–15093.
52 H. J. Sim, Z. Li, P. Xiao and H. Lu, *Molecules*, 2022, **27**, 7840.
53 Y. Sun, A. J. Darling, Y. Li, K. Fujisawa, C. F. Holder, H. Liu, M. J. Janik, M. Terrones and R. E. Schaak, *Chem. Sci.*, 2019, **10**, 10310–10317.